Deep Ultraviolet to Near-Infrared Emission and Photoresponse in Layered N-Doped Graphene Quantum Dots

Libin Tang,[†,‡] Rongbin Ji,[‡] Xueming Li,[§] Gongxun Bai,[†] Chao Ping Liu,[†] Jianhua Hao,[†] Jingyu Lin,[∥] Hongxing Jiang,[∥] Kar Seng Teng,[⊥] Zhibin Yang,[†] and Shu Ping Lau[†,*]

[†]Department of Applied Physics, The Hong Kong Polytechnic University, Hong Kong SAR, [‡]Kunming Institute of Physics, Kunming 650223, Yunnan Province, China, [§]Solar Energy Research Institute, Yunnan Normal University, Kunming 650092, China, [∥]Department of Electrical and Computer Engineering, Texas Tech University, Lubbock, Texas 79409, United States, and [⊥]Multidisciplinary Nanotechnology Center, College of Engineering, Swansea University, Singleton Park, Swansea SA2 8PP, United Kingdom

ABSTRACT Material that can emit broad spectral wavelengths covering deep ultraviolet, visible, and near-infrared is highly desirable. It can lead to important applications such as broadband modulators, photodetectors, solar cells, bioimaging, and fiber communications. However, there is currently no material that meets such desirable requirement. Here, we report the layered structure of nitrogen-doped graphene quantum dots (N-GQDs) which possess broadband emission ranging from 300 to >1000 nm. The broadband emission is attributed to the layered structure of the N-GQDs that contains a large conjugated system and provides extensive delocalized π electrons. In addition, a broadband photodetector with responsivity

as high as 325 V/W is demonstrated by coating N-GQDs onto interdigital gold electrodes. The unusual negative photocurrent is observed which is attributed to the trapping sites induced by the self-passivated surface states in the N-GQDs.

KEYWORDS: graphene quantum dot · nitrogen doping · photoluminescence · broadband emission · photoresponse

Materials that exhibit broadband absorption and emission covering deep ultraviolet (DUV), visible, and near-infrared (NIR) spectral range are of scientific and technological importance due to their valuable applications in the fields of broadband photodetectors, solar cells, and bioimaging. Currently, different semiconductor materials are required to cover these broad spectral ranges. Narrow-gap inorganic semiconductors such as PbS,[1] PbSe,[2] PbTe,[3] HgTe,[4] and InGaAs[5] show infrared optical properties, but their toxicity and chemical instability limit their applications. The wide band gap semiconductors such as ZnO-,[6] GaN-,[7] and AlN[8]-based materials possess UV and DUV optical properties. Although the rare-earth element-doped GaN materials exhibit NIR emission,[9−11] tuning of these materials are difficult for UV applications. Therefore, it is highly desirable to develop a novel functional material that is capable of absorbing and emitting DUV, visible, and NIR spectral wavelengths.

Graphene[12−14] is a hexagonal honeycomb single-layer sp²-bonded carbon material. It exhibits a broadband absorption ranging from 300 to 2500 nm[14] which is beneficial to ultrafast broadband photodetectors.[15,16] Due to its zero band gap, graphene shows no optical emission, and this limits its application in optoelectronic devices. However, graphene quantum dots (GQDs) have emerged as an attractive fluorescence material in the visible and DUV spectral range,[17] but NIR emission has yet to be reported. Nitrogen-doped graphene quantum dots (N-GQDs) are a functional material that can be prepared by a number of methods,[18−22] such as electrochemical,[18] organic synthesis,[19] hydrothermal,[20,21] and self-catalysis.[22] The electrocatalytic activity,[18,19] tunable luminescence,[20] and biocompatibility[20] of N-GQDs have been demonstrated. Here we report a facile "one-pot" microwave-assisted method to prepare N-GQDs using glucose and aqueous ammonia as sources. Most interestingly, the N-GQDs exhibit
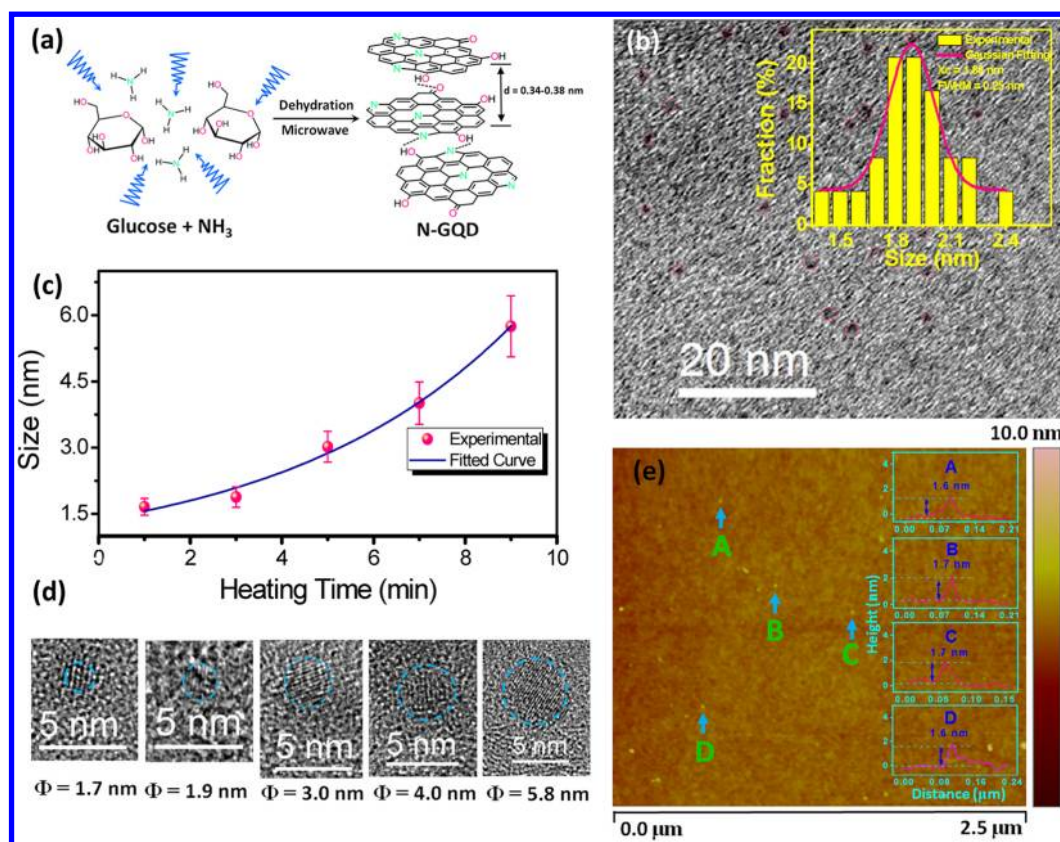
Figure 1. (a) Schematic representation of the synthesis of N-GQDs. (b) TEM image of the N-GQDs (3 min heating) assembled on Cu grid coated with ultrathin amorphous carbon film. Inset: size distribution of the N-GQDs; the red line is the Gaussian fitting curve. (c) Size of the N-GQDs as a function of heating time. (d) Crystalline N-GQDs with sizes of 1.7, 1.9, 3.0, 4.0, and 5.8 nm were grown for 1, 3, 5, 7, and 9 min, respectively. (e) Morphology and height analyses of the N-GQDs as shown in the AFM image; quantum dots A, B, C, and D are randomly chosen N-GQDs.

broadband emission ranging from 300 to >1000 nm. The emission bandwidth of the N-GQDs is one of the widest among all the semiconductor materials and their quantum dot counterparts. The broadband emission is attributed to the layered structure of the N-GQDs which consists of a large conjugated system containing extensive delocalized π electrons. Furthermore, the N-GQDs exhibited broadband photoresponse with unusual negative photocurrent when irradiated by various wavelengths ranging from 365 to 980 nm. Due to the low-cost, chemical stability, as well as the broadband emission and photoresponse properties, the N-GQDs should find important applications in broadband photodetectors, solar cells, bioimaging, and fiber communications.

RESULTS AND DISCUSSION

The monodispersed N-GQDs with various sizes were prepared by microwave-assisted hydrothermal method (MAH) using glucose and aqueous ammonia as sources. The synthetic process is schematically shown in Figure 1a. Glucose provides a carbon source. Ammonia plays two roles in the growth of the N-GQDs; first, it acts as catalyst for the intramolecular and intermolecular dehydration of glucose, and second, it is for N doping.

The TEM image of the N-GQDs prepared at a growth time of 3 min is shown in Figure 1b. The prepared N-GQDs show monodispersed distribution. The N-GQDs highlighted by the red dashed circles reveal the uniformity in size. The size distribution obeys a Gaussian distribution; the most probable size is 1.9 nm with a full width at-half-maximum (fwhm) of 0.25 nm. The size of the N-GQDs increases with increasing heating time; for example, as the growth time increases from 1 to 9 min, the diameter of the N-GQDs increases from 1.7 to 5.8 nm. The heating time dependence accords with an exponential growth process, as shown in Figure 1c. The crystalline structures of the N-GQDs with sizes of 1.7, 1.9, 3.0, 4.0, and 5.8 nm prepared at the heating time of 1, 3, 5, 7, and 9 min, respectively, are shown in Figure 1d. In order to investigate the morphology and the height of the N-GQDs, atomic force microscopy (AFM) characterization was performed, as shown in Figure 1e for N-GQDs grown for 3 min. The dots A, B, C, and D indicated by the blue arrows are randomly chosen N-GQDs, and their heights range from 1.6 to 1.7 nm (inset of Figure 1e), which are very close to the size of the N-GQDs (1.88 nm) as characterized using TEM.

Figure 2a is the high-resolution transmission electron microscopy (HRTEM) image of N-GQD prepared by
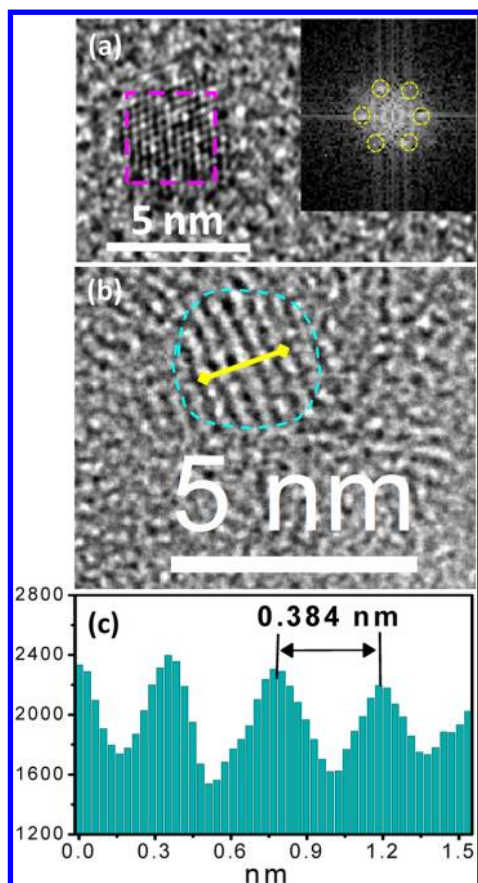
Figure 2. (a) HRTEM image of a typical N-GQD. Inset: fast Fourier transform image of a selected area (pink square), the hexagonal honeycomb structure, is indicated. (b) HRTEM image and the (c) line profile of the selected N-GQD. The layered structure with an interlayer spacing of 0.384 nm is observed. The sample was prepared by microwave heating for 5 min.

5 min heating. The lattice fringes of the N-GQD can be clearly observed. The fast Fourier transform of the selected area (pink square) is shown in the inset of Figure 2a, revealing the hexagonal crystalline structure. The N-GQD also reveals a layered structure (Figure 2b) with an interlayer spacing of ∼0.38 nm (Figure 2c), which is slightly larger than that of bulk graphite (0.335 nm)[23,24] due to the presence of the functional groups that enlarge the basal plane spacing of the N-GQDs.

The detailed TEM structural characterization of the N-GQDs can be found in Supporting Information (SI, Figures S1−S5), which reveal the high-crystal quality of the N-GQDs. The electron energy loss spectroscopy (EELS)[17,25−29] and low-loss EELS of the N-GQDs were studied, and the detailed discussion can be found in SI (Figure S6 and Figure S7, respectively).

X-ray photoelectron spectroscopy (XPS)[30,31] was performed on the samples to investigate the chemical bonding of the N-GQDs. Figure S8a of SI shows the N 1s XPS spectra as a function of size. Three types of N-related bonding can be identified, namely, pyridinic
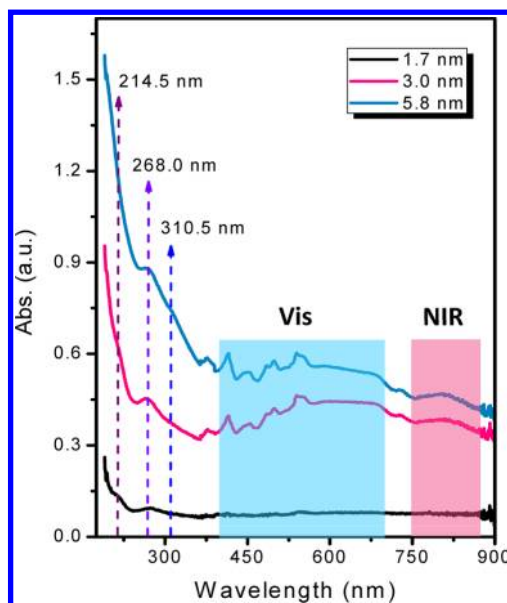

Figure 3. UV−vis−NIR absorption spectra of the N-GQDs at various sizes.

N (∼399.2 eV), pyrrolic N (∼400.2 eV), and graphitic N (∼401.6 eV). These peaks are also observed in N-GQDs prepared by self-catalysis method.[22] The C 1s XPS spectra are shown in Figure S8b of SI. The spectra can be deconvoluted into five peaks centered at around 284.5 eV (C═C), 285.8 eV (C−C, C−H, C═N), 286.6 eV (C−OH), 287.2 eV (C−O−C, C−N), and 288.6 eV (C═O), revealing different types of bonding to C. The atomic N/C ratio of the N-GQDs (Φ = 3.0 nm) is determined to be 8.3/100, indicating that C is the dominant element. The N/C atomic ratio (8.3%) is much higher than that of various N-doped graphene-based materials (0.3−5.6%).[21,32,33] The N-GQDs were further characterized by X-ray diffraction (XRD), Fourier transform infrared (FTIR) spectroscopy, and Raman spectroscopy as discussed in SI (Figure S9).

The UV−vis−NIR absorption spectra of the N-GQDs are shown in Figure 3. There are three UV absorption peaks located at 214.5, 268.0, and 310.5 nm. The UV absorption peaks are related to the electron transitions from π (or n) to π^* of C═C, C═N, and C═O. It is worth noting that the N-GQDs with diameter larger than 1.7 nm exhibit a broad visible absorption. The visible absorption band between 400 and 700 nm is highlighted in blue in Figure 3. Thus, the origin of visible absorption of the N-GQDs could be related to the partial conjugated π electrons in the layered N-GQDs. Importantly, a broad NIR absorption band peaking at ∼812 nm becomes noticeable as the size of the N-GQDs reaches 3.0 nm. The NIR absorption could be attributed to the larger conjugated system containing extensive delocalized π electrons in the layered N-GQDs. The UV−vis−NIR absorption spectra suggest that the layered structure of the N-GQDs with relatively larger size (∼3.0 nm) can lead to visible and NIR

absorption which is due to an increase in conjugated π electrons in the structure.

The photoluminescence (PL) quantum yields (QYs) of the N-GQDs with various diameters were determined to be between 6.8 and 11.3% using an absolute QY measurement method.[17] The excitation wavelength (λ_E) of 375 nm was used, and the emission spectra were measured between 400 and 700 nm. The PL excitation (PLE) spectra of the N-GQDs are shown in Figure S10 of SI. Three bands are located at 239, 269, and 333 nm. These peaks correspond to the electron transitions from π (or n) to π^* of C=C, C=N, and C=O. Clearly, these values are close to those of the UV absorptions, showing that the electron transitions for double bonds in the N-GQDs occur in the UV range. Importantly, the N-GQDs exhibit broadband PL peaked at 302, 542, and 915 nm when excited by wavelengths of 197, 475, and 808 nm, respectively, as shown in Figure 4. This is the first graphene-based material which exhibits broadband PL covering the entire DUV—visible—NIR spectral range.

Figure 5a shows the PL spectra of the N-GQDs at various sizes using a 197 nm laser as an excitation

source measured at 300 K. The size of the N-GQDs does not apparently influence the DUV peak centered at ~302 nm (PL spectra measured at 10 K are shown in Figure S11 of SI). The size-independent DUV peak may be due to the localized π electrons of the C-based double bonds (mainly C=C) in the N-GQDs. In addition to the DUV emission, we also observed a visible light emission (>400 nm) that resulted from the radiative recombination after interband transition that converts DUV absorption to visible light emission. Figure 5b shows the size-dependent visible PL emission of the N-GQDs excited by 375 nm laser. For the N-GQDs with a diameter of 1.7 nm, the emission peak is centered at 450 nm. The emission peak red shifts as the size increases. The wavelength reaches 582 nm when the size equals 5.8 nm. Figure 5c shows the NIR PL spectra of the N-GQDs excited by a laser with a wavelength of 808 nm. If the size of the N-GQDs is too small (~1.7 nm), no obvious NIR emission can be observed, probably due to the small conjugated system which contains fewer delocalized π electrons. As the size of the N-GQDs increased to ≥3.0 nm, there are two NIR emissions peaked at ~862 and ~917 nm. These emissions are attributed to free and bound excitons. The bound excitons were bound to the surface states (defects), requiring additional coulomb energies which make the bound excitons energy lower (i.e., 917 nm) than that of the free excitons (862 nm). Importantly, the NIR emission peaks can be further tuned to a longer wavelength when the N-GQD was excited by a light source with longer wavelength, as shown in Figure S12 of SI. The NIR emission peaks at ~1017 and ~1060 nm can be observed when the N-GQDs were excited by a laser of 980 nm. Similar to the typical GQDs, the N-GQDs also exhibited excitation wavelength (λ_{Ex})-dependent PL, as shown in Figure S13a of SI. Both the PL intensity and emission peak position changes with λ_{Ex} (Figure S13b of SI).[26]
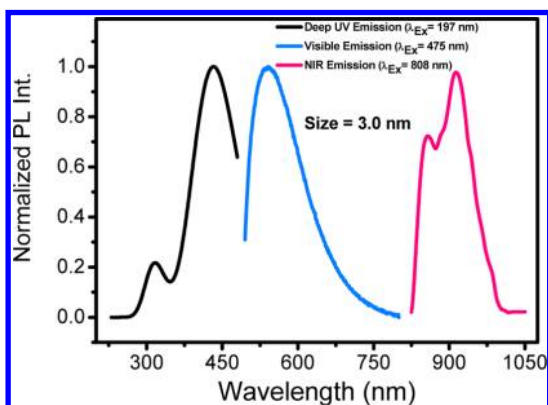

Figure 4. Normalized PL spectra of the N-GQDs (Φ = 3.0 nm) excited by various wavelengths.
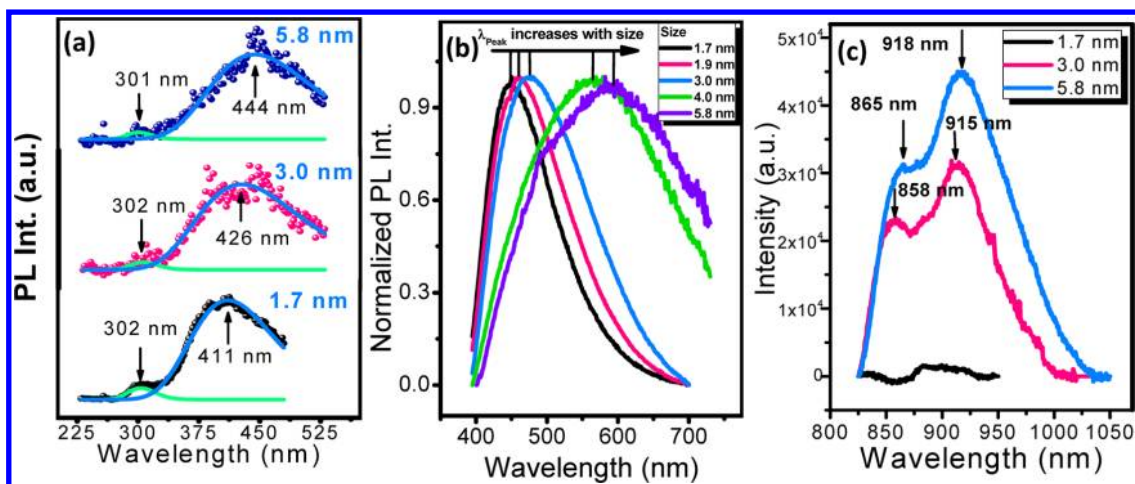

Figure 5. PL spectra of the N-GQDs with different sizes. (a) Deep UV PL spectra of the N-GQDs excited by 197 nm laser measured at 300 K. (b) Size-dependent visible PL spectra of N-GQDs excited by 375 nm laser. (c) NIR PL spectra of the N-GQDs excited by 808 nm laser.
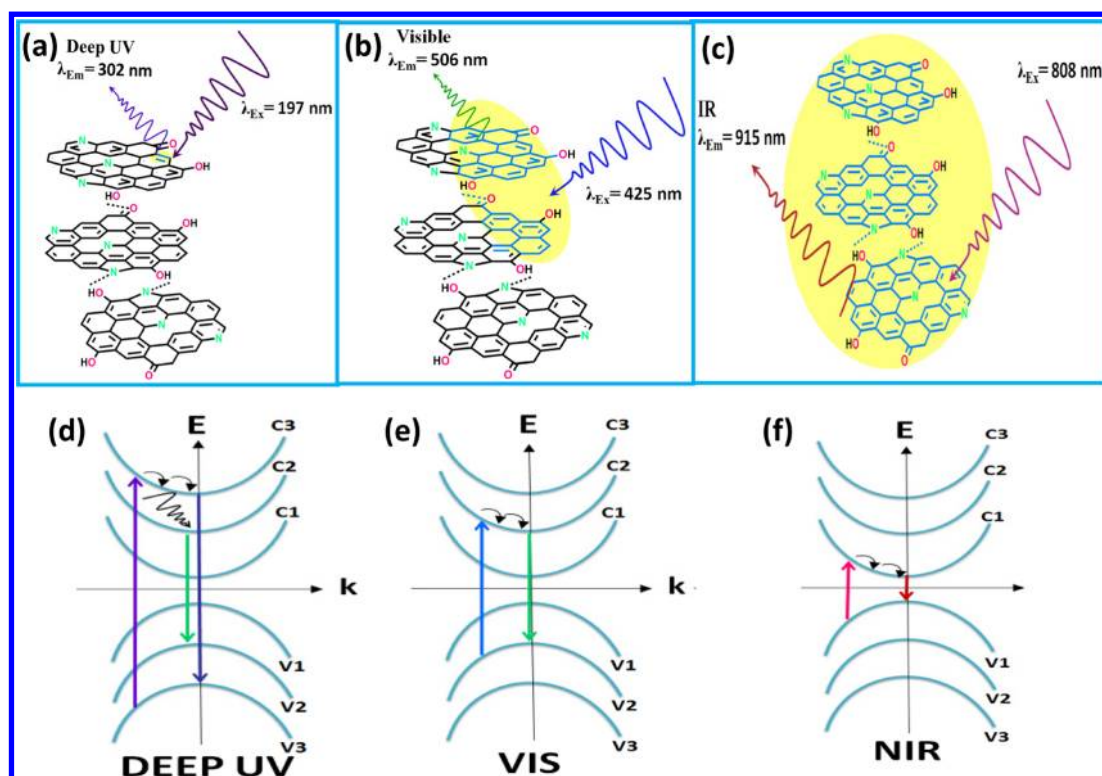
Figure 6. Mechanism for the broadband emission in the N-GQDs. (a) DUV absorption by localized π electron in carbon-based double bonds (mainly C=C), the DUV PL emission, and visible light PL emission occur after vibration relaxation and interband transition shown in (d). (b) Visible light absorption by partial conjugated π electrons in the layered structure of the GQDs; the λ_{Ex}-dependent visible light PL emission occurs after vibration relaxation as shown in (e). (c) NIR absorption by a larger conjugated system containing more π electrons in the layered structure of the N-GQDs; the NIR PL emission occurs after vibration relaxation as shown in (f).

Based on the information on the structural, absorption, and PL properties, the mechanism of the broadband emission covering DUV, visible, and NIR range can be explained as follows. Figure 6 shows the schematic diagrams of the broadband emission mechanism of the N-GQDs excited by various wavelengths. As for the DUV emission, the absorption of DUV photons by the localized π electron in double bonds (mainly C=C) produces an electron–hole pair (exciton) after electron transition ($v_3 \to c_3$). The exciton may emit DUV light ($c_3 \to v_3$) through radiative recombination after vibration relaxation (Figure 6d). The excited electron may also undergo interband transition from a higher conduction band to a lower conduction band (e.g., $c_3 \to c_2$), subsequently emitting visible light ($c_2 \to v_2$) by radiative recombination. This could be the reason why the DUV absorption resulted in both DUV and visible emission, as shown in Figure 5a. As far as visible emission is concerned, the partial conjugated π electrons in the layered structure of the N-GQD (Figure 6b) play a major role. The visible light absorption ($v_2 \to c_2$) of the partial conjugated π electrons may result in excitons that can emit visible light ($c_2 \to v_2$) (Figure 6e) after the vibration relaxation which emits the photons with wavelengths longer than the absorbed wavelengths. A longer excitation wavelength is needed for a larger conjugated π electron system in order to

satisfy the most probable absorption, resulting in excitation wavelength-dependent (λ_{Ex}) emission. In the case of NIR emission, the conjugated π electrons in the layered structure of the N-GQDs facilitate the NIR absorption (Figure 6c), and the vibration relaxation should also occur since the wavelength of the emitted NIR light (e.g., 915 nm) (Figure 6f) is longer than the wavelength of the absorbed NIR photons (808 nm). Apparently, only those N-GQDs with sizes reaching 3.0 nm can absorb and emit NIR light. The layered structure assists the process due to the extensive conjugated π electron system. It is reported that π electrons[34] and large macromolecular domains[35] are also related to the NIR PL mechanism observed in graphene oxide (GO).

The time-resolved PL decay measurements were performed on the N-GQDs. A triple-exponential equation[17,36,37] is fitted well to the experimental data, and the PL lifetime contains a fast component (τ_1: 0.61–1.38 ns) and two slow components (τ_2: 2.18–4.13 ns and τ_3 >10 ns). The size-dependent PL decay curves at a fixed excitation wavelength λ_{Ex} (375 nm) and emission wavelength λ_{Em} (570 nm) are shown in Figure S14 of SI. It is found that the larger the N-GQDs, the faster the decay time. The average lifetimes and other fitting parameters for different N-GQD sizes are listed in Table S1 of SI. The average lifetime strongly depends
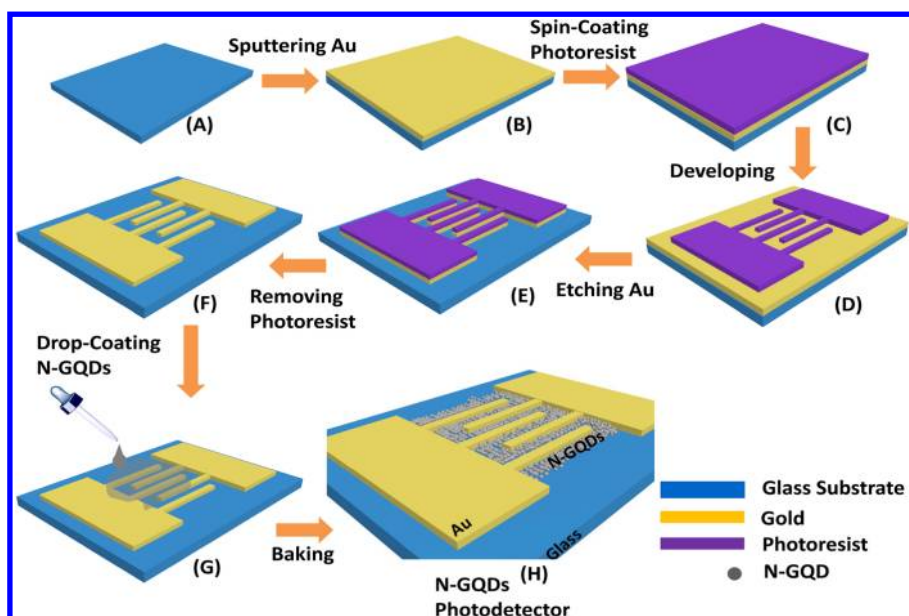
Figure 7. Schematic diagrams illustrating the fabrication process of the N-GQDs photodetector.

on the size of the N-GQDs. In order to reveal the size-dependent lifetime of the N-GQDs, the lifetime *versus* λ_{Em} for various sizes is plotted and shown in Figure S15a. It is evident that a larger size N-GQD results in a shorter lifetime for a fixed λ_{Em}. It can also be observed that the peak of the lifetime (maximum lifetime) increases with increasing N-GQD size. The above-mentioned properties should correlate to the presence of N in the quantum dots. It is worth mentioning that, under the same conditions (λ_{Ex} = 375 nm, λ_{Em} = 470 nm), the average lifetimes of various N-GQD sizes are smaller than that of nitrogen-free GQDs.[26] It suggests that the presence of N may effectively accelerate the process of emitting the photon after absorption, which results from the "bridge effect" of N.[22] Combined with the structural information disclosed by XPS, the diversity of N configuration (pyridinic, pyrrolic, and graphitic N) is beneficial to the formation of a conjugated π electron system which may be responsible for the broadband emission in the N-GQDs.

In order to obtain an in-depth understanding on the relationship between the PL lifetime and the size of the N-GQDs, a plot of lifetime *versus* diameter of the N-GQDs is shown in Figure S16a (SI). Evidently, an exponential decay curve is found. As mentioned above, the lifetime of the N-GQDs exhibits a "peak-like" dependence on λ_{Em} which is similar to the dependence of PL emission intensity on wavelength. Both of the curves are similar in shape but different in value (Figure S16b of SI). Under the same λ_{Ex} of 375 nm, the PL emission peaked at 476 nm (Φ = 3.0 nm); the lifetime curve, however, peaked at 582 nm, resulting in a red shift of 106 nm. It can also be seen that the fwhm value of the lifetime curve (fwhm = 230 nm) is wider than that of the emission curve (fwhm = 154 nm). The above differences in peak

position and fwhm might be related to the doping and unique structure of the N-GQDs.

The N-GQDs also exhibit broad color tunability. Figure S15b shows the photographs of the N-GQDs with different sizes under ambient (top) and 365 nm UV light (bottom) illumination. To illustrate the emission properties of the N-GQDs, DI water is used as a control sample. Clearly, the larger the size of the N-GQDs, the darker the color of the solution. The N-GQDs can emit a variety of colors under UV light illumination, including blue, green-blue, white, green-yellow, and orange. The chromaticity coordinates of the N-GQDs at different sizes were determined using a laser of 375 nm as the excitation source. As shown in Figure S15c, the letters A, B, C, D, and E denote the size of the N-GQDs of 1.7, 1.9, 3.0, 4.0, and 5.8 nm, respectively. Interestingly, a variety of emission colors can be obtained as the size of the N-GQDs increases from 1.7 to 5.8 nm, for example, blue (A, 1.7 nm), green-blue (B, 1.9 nm), white (C, 3.0 nm), green-yellow (D, 4.0 nm), and orange (E, 5.8 nm). The corresponding chromaticity coordinates are listed in the inset of Figure S15c. The emission colors cover three primitive colors; therefore, in principle, it is possible to emit a variety of colors by mixing different sizes of N-GQDs. This should find application in light converters.[17]

The observed broadband emission properties in the N-GQDs have prompted us to study the photoresponse of the N-GQDs under various irradiation wavelengths. Figure 7 illustrates the fabrication processes of the N-GQD-based photodetectors using interdigital gold electrodes. The N-GQD solution was drop-coated onto the interdigital electrodes, followed by heating at 90 °C for 15 min to stiffen the N-GQD films on a hot plate in the air. The schematic diagram of the N-GQD-based photodetector is shown in Figure 8a.
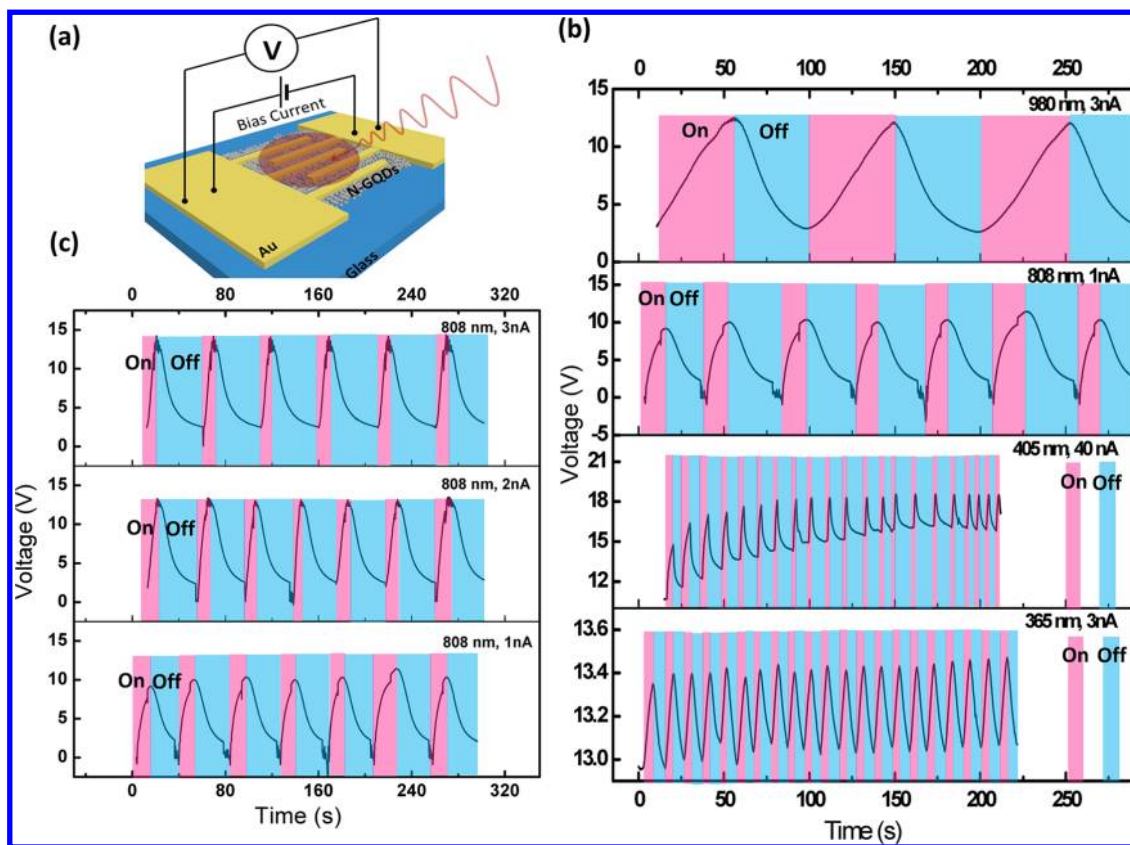
Figure 8. (a) Schematic diagram of the N-GQDs photodetector. (b) Photoresponse of the N-GQDs (Φ = 4.0 nm) with various light sources. (c) Photovoltage responses with various bias currents.

Different from conventional photodetectors, the N-GQDs exhibit negative photocurrent when irradiated to light, as shown in Figure S17 of SI. When the light is turned on, the current is decreased rather than increased. When the light is off, the current is restored to its original level. In order to show the positive photoresponse of the N-GQDs, we measured the photovoltage of the detectors by applying a bias current to the detector. Figure 8b shows the photovoltage response of the detector when irradiated with UV (365 nm, light-emitting diode), visible (405 nm, laser), and NIR (808 and 980 nm, laser) light sources. The N-GQD photodetector can respond to UV and NIR. The response time is about 50 s for 980 nm and reduced to about 10 s for 365 nm. The performance parameters of the N-GQD photodetector are listed in Table S2 of SI. The induced photovoltage (V_{photo}) is the voltage difference between the peak (V_{peak}) and valley (V_{valley}) when light is turned on and off, respectively. The on–off ratio is defined as V_{peak}/V_{valley}. The voltage responsivity (R_v) is calculated as V_{photo}/P_{light}, where P_{light} is the power of the light source.[38] The on–off ratios of 808 and 980 nm are 6.49 and 4.29, respectively, and the values are much larger than 1. The responsivities for various light sources are 4.79 V/W (980 nm), 10.91 V/W (808 nm), 325.00 V/W (405 nm), and 1.14 V/W (365 nm). The responsivity values are larger than that of carbon-nanotube-based broadband photodetector (0.9–1.8 V/W) with similar spectral range.[38] The effect of bias current on the photovoltage response of the N-GQD detector is shown in Figure 8c. The responsivity increases linearly from 10.91 to 14.08 V/W as bias current increases from 1 to 3 nA (Figure S18 and Table S2 of SI). It should be noted that the performance of the photodetector has not been optimized yet. Based on the emission results, the photodetector may also respond to wavelengths below 365 nm and >1000 nm.

The observed photoresponse from the N-GQD-based detector can be explained as follows. The absorption of photon (UV–vis–NIR) may generate excited electron–hole pairs (excitons) which cannot freely move due to the presence of a passivated surface layer (functional groups) on the surface of the N-GQDs as revealed by XPS and FTIR. The bound electron–hole pairs may trap charge carriers when the N-GQDs are exposed to light, forming photoinduced charge traps (Figure S19 of SI). Under a bias current, due to the presence of photoinduced traps in the N-GQDs, the charge carriers may be trapped drastically as they passed through the N-GQDs (Figure S20 of SI); in order to maintain a constant current, the trapped charges will be compensated by increasing voltage, resulting in increasing photovoltage.

CONCLUSIONS

The broadband emission from the N-GQDs covering 300 to >1000 nm was demonstrated. The broadband optical properties of the N-GQDs are attributed to the layered structure of the N-GQDs which create a large conjugated system containing extensive delocalized π electrons. The DUV emission comes from the localized π electron in double bonds (mainly C=C). The visible emission is caused by the partial conjugated π electrons in the N-GQDs. As for NIR emission, the conjugated π electrons in the layered structure of the N-GQDs facilitate the NIR absorption. Furthermore, the N-GQDs exhibited photoresponse from 365 to 980 nm with responsivity as high as 325 V/W at 405 nm. The unique broadband emission and photoresponse of the layered N-GQDs may lead to applications in a wide range of optoelectronic devices including photodetectors, solar cells, and light-emitting devices.

METHODS

N-GQD Preparation. One gram of glucose was dissolved in 7.5 mL of deionized (DI) water, followed by adding 0.5 mL of aqueous ammonia. After the solution was mixed, it was diluted 5-fold with DI water. Then 2.5 mL of the source solution was taken out into a glass bottle. The solution was heated in a microwave oven at 280 W for 1, 3, 5, 7, and 9 min to grow a series of N-GQDs with various diameters. The N-GQD samples were dialyzed by molecular weight cutoff (MWCO) of 1000 against DI water for characterization. The yield of the N-GQDs was determined to be around ∼78%.

Characterizations. TEM, HRTEM, HAADF-STEM, EDS, EELS, and low-loss EELS were performed on JEOL, JEM-2100F, at an operating voltage of 200 kV. The morphology and height characterizations of the N-GQDs were performed by AFM (Digital Instruments NanoScope IV) operating in the tapping mode at room temperature. The FTIR spectra of the samples were obtained using the KBr pellet method by Nicolet Magna-IR 760 spectrometer with a resolution of 4 cm^{-1}. Raman scattering spectra were obtained using Horiba JobinYvon HR800 spectrometer at room temperature with a laser of 488 nm wavelength. XPS experiment was performed using Al Kα source, having an energy of 1486.6 eV at room temperature with the VG ESCAlab MKII. XRD was carried out with a Rigaku SmartLab X-ray diffractometer (Cu Kα radiation λ = 1.54056 Å) operating at 45 kV and 200 mA. The UV−vis spectra were recorded at room temperature on a Shimadzu UV-2550 UV−vis spectrophotometer. The PL characterizations including excitation spectra, time-resolved PL, as well as quantum yields of the N-GQDs were recorded using an FLS920P Edinburgh Analytical Instrument apparatus. For the excitation-dependent emission spectra and PLE spectra, a Xe lamp was used as an excitation source. The NIR emission spectra of the N-GQDs were measured using an 808 nm laser as excitation source. The DUV emission spectra of the N-GQD films were investigated by employing a specially designed time-resolved DUV laser spectroscopy system consisting of a frequency-tripled (266 nm) and quadrupled (197 nm) Ti:sapphire laser (100 fs) with a 76 MHz repetition rate. A streak camera with a time resolution of 2 ps was used for recording time-resolved PL. The absolute quantum yield measurements were carried out using an integrating sphere (Edinburgh Instruments, 150 mm in diameter coated with barium sulfate). The N-GQD samples were diluted with DI water to avoid reabsorption; the samples were placed in the cuvettes inside the integrating sphere. The time-resolved PL spectra of the N-GQDs were recorded using 375 nm picosecond pulsed laser (model EPL375, Edinburgh Instruments) as an excitation source. The photoresponse measurements were carried out using a computer-controlled Keithley 2400 sourcemeter connected to a probe station.

Conflict of Interest: The authors declare no competing financial interest.

Supporting Information Available: Detailed information on chemicals, fabrication of photodetectors, structural characterization of N-GQD by TEM, EELS, low-loss EELS, XRD, FTIR, and Raman, optical characterization by PL, PLE, time-resolved PL, chromaticity coordinates, and the mechanism for photoresponse. This material is available free of charge *via* the Internet at http://pubs.acs.org.

REFERENCES AND NOTES

1. Mcdonald, S. A.; Konstantatos, G.; Zhang, S.; Cyr, P. W.; Klem, E. J. D.; Levina, L.; Sargent, E. H. Solution-Processed PbS Quantum Dot Infrared Photodetectors and Photovoltaics. *Nat. Mater.* **2005**, *4*, 138–142.

2. Talapin, D. V.; Murray, C. B. PbSe Nanocrystal Solids for n- and p-Channel Thin Film Field-Effect Transistors. *Science* **2005**, *310*, 86–89.

3. Urban, J. J.; Talapin, D. V.; Shevchenko, E. V.; Kagan, C. R.; Murray, C. B. Synergism in Binary Nanocrystal Superlattices Leads to Enhanced p-Type Conductivity in Self-Assembled PbTe/Ag$_2$Te Thin Films. *Nat. Mater.* **2007**, *6*, 115–121.

4. Keuleyan, S.; Lhuillier, E.; Guyot-Sionnest, P. Synthesis of Colloidal HgTe Quantum Dots for Narrow Mid-IR Emission and Detection. *J. Am. Chem. Soc.* **2011**, *133*, 16422–16424.

5. Patel, R. B.; Bennett, A. J.; Farrer, I.; Nicoll, C. A.; Ritchie, D. A.; Shields, A. J. Two-Photon Interference of the Emission from Electrically Tunable Remote Quantum Dots. *Nat. Photonics* **2010**, *4*, 632–635.

6. Soci, C.; Zhang, A.; Xiang, B.; Dayeh, S. A.; Aplin, D. P. R.; Park, J.; Bao, X. Y.; Lo, Y. H.; Wang, D. ZnO Nanowire UV Photodetectors with High Internal Gain. *Nano Lett.* **2007**, *7*, 1003–1009.

7. Li, D.; Sun, X.; Song, H.; Li, Z.; Chen, Y.; Jiang, H.; Miao, G. Realization of a High-Performance GaN UV Detector by Nanoplasmonic Enhancement. *Adv. Mater.* **2012**, *24*, 845–849.

8. Oto, T.; Banal, R. G.; Kataoka, K.; Funato, M.; Kawakami, Y. 100 mW Deep-Ultraviolet Emission from Aluminium-Nitride-Based Quantum Wells Pumped by an Electron Beam. *Nat. Photonics* **2010**, *4*, 767–771.

9. Hömmerich, U.; Nyein, E. E.; Lee, D. S.; Heikenfeld, J.; Steckl, A. J.; Zavada, J. M. Photoluminescence Studies of Rare Earth (Er, Eu, Tm) *In Situ* Doped GaN. *Mater. Sci. Eng.* **2003**, *B105*, 91–96.

10. Kim, J. H.; Holloway, P. H. Near-Infrared Electroluminescence at Room Temperature from Neodymium-Doped Gallium Nitride Thin Films. *Appl. Phys. Lett.* **2004**, *85*, 1689–1691.

11. Kim, J. H.; Holloway, P. H. Near-Infrared-Electroluminescent Light-Emitting Planar Optical Sources Based on Gallium Nitride Doped with Rare Earths. *Adv. Mater.* **2005**, *17*, 91–96.

12. Novoselov, K. S.; Geim, A. K.; Morozov, S. V.; Jiang, D.; Zhang, Y.; Dubonos, S. V.; Grigorieva, I. V.; Firsov, A. A. Electric Field Effect in Atomically Thin Carbon Films. *Science* **2004**, *306*, 666–669.

13. Li, X.; Cai, W.; An, J.; Kim, S.; Nah, J.; Yang, D.; Piner, R.; Velamakanni, A.; Jung, I.; Tutuc, E.; Banerjee, S. K.; Colombo, L.; Ruoff, R. S. Large-Area Synthesis of High-Quality and Uniform Graphene Films on Copper Foils. *Science* **2009**, *324*, 1312–1314.

14. Bonaccorso, F.; Sun, Z.; Hasan, T.; Ferrari, A. C. Graphene Photonics and Optoelectronics. *Nat. Photonics* **2010**, *4*, 611–622.

15. Xia, F.; Mueller, T.; Lin, Y.-M.; Valdes-Garcia, A.; Avouris, P. Ultrafast Graphene Photodetector. *Nat. Nanotechnol.* **2009**, *4*, 839–843.

16. Urich, A.; Unterrainer, K.; Mueller, T. Intrinsic Response Time of Graphene Photodetectors. *Nano Lett.* **2011**, *11*, 2804–2808.

17. Tang, L.; Ji, R.; Cao, X.; Lin, J.; Jiang, H.; Li, X.; Teng, K. S.; Luk, C. M.; Zeng, S.; Hao, J.; Lau, S. P. Deep Ultraviolet Photoluminescence of Water-Soluble Self-Passivated Graphene Quantum Dots. *ACS Nano* **2012**, *6*, 5102–5110.

18. Li, Y.; Zhao, Y.; Cheng, H.; Hu, Y.; Shi, G.; Dai, L.; Qu, L. Nitrogen-Doped Graphene Quantum Dots with Oxygen-Rich Functional Groups. *J. Am. Chem. Soc.* **2012**, *134*, 15–18.

19. Li, Q.; Zhang, S.; Dai, L.; Li, L.-S. Nitrogen-Doped Colloidal Graphene Quantum Dots and Their Size-Dependent Electrocatalytic Activity for the Oxygen Reduction Reaction. *J. Am. Chem. Soc.* **2012**, *134*, 18932–18935.

20. Hu, C.; Liu, Y.; Yang, Y.; Cui, J.; Huang, Z.; Wang, Y.; Yang, L.; Wang, H.; Xiao, Y.; Rong, J. One-Step Preparation of Nitrogen-Doped Graphene Quantum Dots from Oxidized Debris of Graphene Oxide. *J. Mater. Chem. B* **2013**, *1*, 39–42.

21. Li, M.; Wu, W.; Ren, W.; Cheng, H.-M.; Tang, N.; Zhong, W.; Du, Y. Synthesis and Upconversion Luminescence of N-Doped Graphene Quantum Dots. *Appl. Phys. Lett.* **2012**, *101*, 103107.

22. Tang, L.; Ji, R.; Li, X.; Teng, K. S.; Lau, S. P. Energy-Level Structure of Nitrogen-Doped Graphene Quantum Dots. *J. Mater. Chem. C* **2013**, *1*, 4908–4915.

23. Oshima, C.; Nagashima, A. Ultra-thin Epitaxial Films of Graphite and Hexagonal Boron Nitride on Solid Surfaces. *J. Phys.: Condens. Matter* **1997**, *9*, 1–20.

24. Biedermann, L. B.; Bolen, M. L.; Capano, M. A.; Zemlyanov, D.; Reifenberger, R. G. Insights into Few-Layer Epitaxial Graphene Growth on 4H-SiC(000) Substrates from STM Studies. *Phys. Rev. B* **2009**, *79*, 125411.

25. Gass, M. H.; Bangert, U.; Bleloch, A. L.; Wang, P.; Nair, R. R.; Geim, A. K. Free-Standing Graphene at Atomic Resolution. *Nat. Nanotechnol.* **2008**, *3*, 676–681.

26. Tang, L.; Ji, R.; Li, X.; Teng, K. S.; Lau, S. P. Size-Dependent Structural and Optical Characteristics of Glucose-Derived Graphene Quantum Dots. *Part. Part. Syst. Charact.* **2013**, *30*, 523–531.

27. Li, X.; Lau, S. P.; Tang, L.; Ji, R.; Yang, P. Multicolour Light Emission from Chlorine-Doped Graphene Quantum Dots. *J. Mater. Chem. C* **2013**, *1*, 7308–7313.

28. Ci, L.; Song, L.; Jin, C.; Jariwala, D.; Wu, D.; Li, Y.; Srivastava, A.; Wang, Z. F.; Storr, K.; Balicas, L.; Liu, F.; Ajayan, P. M. Atomic Layers of Hybridized Boron Nitride and Graphene Domains. *Nat. Mater.* **2010**, *9*, 430–435.

29. Mkhoyan, K. A.; Contryman, A. W.; Silcox, J.; Stewart, D. A.; Eda, G.; Mattevi, C.; Miller, S.; Chhowalla, M. Atomic and Electronic Structure of Graphene-Oxide. *Nano Lett.* **2009**, *9*, 1058–1063.

30. Kim, S.; Zhou, S.; Hu, Y.; Acik, M.; Chabal, Y. J.; Berger, C.; Heer, W.; Bongiorno, A.; Riedo, E. Room-Temperature Metastability of Multilayer Graphene Oxide Films. *Nat. Mater.* **2012**, *11*, 544–549.

31. Tang, L.; Li, X.; Ji, R.; Teng, K. S.; Tai, G.; Ye, J.; Wei, C.; Lau, S. P. Bottom-Up Synthesis of Large-Scale Graphene Oxide Nanosheets. *J. Mater. Chem.* **2012**, *22*, 5676–5683.

32. Zhang, C.; Fu, L.; Liu, N.; Liu, M.; Wang, Y.; Liu, Z. Synthesis of Nitrogen-Doped Graphene Using Embedded Carbon and Nitrogen Sources. *Adv. Mater.* **2011**, *23*, 1020–1024.

33. Panchakarla, L. S.; Subrahmanyam, K. S.; Saha, S. K.; Govindaraj, A.; Krishnamurthy, H. R.; Waghmare, U. V.; Rao, C. N. R. Synthesis, Structure, and Properties of Boron- and Nitrogen-Doped Graphene. *Adv. Mater.* **2009**, *21*, 4726–4730.

34. Luo, Z.; Vora, P. M.; Mele, E. J.; Johnson, A. T. C.; Kikkawa, J. M. Photoluminescence and Band Gap Modulation in Graphene Oxide. *Appl. Phys. Lett.* **2009**, *94*, 111909.

35. Sun, X.; Liu, Z.; Welsher, K.; Robinson, J. T.; Goodwin, A.; Zaric, S.; Dai, H. Nano-graphene Oxide for Cellular Imaging and Drug Delivery. *Nano Res.* **2008**, *1*, 203–212.

36. Peng, J.; Gao, W.; Gupta, B. K.; Liu, Z.; Romero-Aburto, R.; Ge, L.; Song, L.; Alemany, L. B.; Zhan, X.; Gao, G.; Vithayathil, S. A.; Kaipparettu, B. A.; Marti, A. A.; Hayashi, T.; Zhu, J.-J.; Ajayan, P. M. Graphene Quantum Dots Derived from Carbon Fibers. *Nano Lett.* **2012**, *12*, 844–849.

37. Bao, L.; Zhang, Z. L.; Tian, Z. Q.; Zhang, L.; Liu, C.; Lin, Y.; Qi, B. P.; Pang, D. W. Electrochemical Tuning of Luminescent Carbon Nanodots: From Preparation to Luminescence Mechanism. *Adv. Mater.* **2011**, *23*, 5801–5806.

38. St-Antoine, B. C.; Ménard, D.; Martel, R. Single-Walled Carbon Nanotube Thermopile for Broadband Light Detection. *Nano Lett.* **2011**, *11*, 609–613.

ARTICLE